

Final Draft
of the original manuscript:

Yasakau, K.A.; Giner, I.; Vree, C.; Ozcan, O.; Grothe, R.; Oliveira, A.;
Grundmeier, G.; Ferreira, M.G.S.; Zheludkevich, M.L.:

**Influence of stripping and cooling atmospheres on surface
properties and corrosion of zinc galvanizing coatings**

In: Applied Surface Science (2016) Elsevier

DOI: 10.1016/j.apsusc.2016.07.093

Influence of stripping and cooling atmospheres on surface properties and corrosion of zinc galvanizing coatings

K.A. Yasakau^{*1}, I. Giner², C. Vree³, O. Ozcan², R. Grothe², A. Oliveira¹, G. Grundmeier², M.G.S. Ferreira¹, M.L. Zheludkevich^{1,4}.

¹ Department of Materials and Ceramic Engineering, CICECO – Aveiro Institute of Materials, University of Aveiro, 3810-193 Aveiro, Portugal.

² Universität Paderborn, Fakultät NW - Department Chemie, Technische und Makromolekulare Chemie Warburger Strasse 100 D-33098 Paderborn.

³ Salzgitter Mannesmann Forschung, GmbH Division Surface Technology Eisenhüttenstrasse 99 38239, Salzgitter, Germany.

⁴ Department of Corrosion and Surface Technology, Institute of Materials Research Helmholtz-Zentrum Geesthacht, Max-Planck Str. 1, 21502 Geesthacht, Germany.

Abstract

In this work the influence of stripping/cooling atmospheres used after withdrawal of steel sheet from Zn or Zn-alloy melt on surface properties of Zn (Z) and Zn-Al-Mg (ZM) hot-dip galvanizing coatings has been studied. The aim was to understand how the atmosphere (composed by nitrogen (N₂) or air) affects adhesion strength to model adhesive and corrosive behaviour of the galvanized substrates. It was shown that the surface chemical composition and Volta potential of the galvanizing coatings prepared under the air or nitrogen atmosphere are strongly influenced by the atmosphere. The surface chemistry Z and ZM surfaces prepared under N₂ contained a higher content of metal atoms and a richer hydroxide density than the specimens prepared under air atmosphere as assessed by X-ray photoelectron spectroscopy (XPS). The induced differences on the microstructure of the galvanized coatings played a key role on the local corrosion induced defects as observed by means of In situ Atomic force microscopy (AFM). Peel force tests performed on the substrates coated by model adhesive films indicate a higher adhesive strength to the surfaces prepared under nitrogen atmosphere. The obtained results have been discussed in terms of the microstructure and surface chemical composition of the galvanizing coatings.

Keywords: zinc galvanizing coating; adhesion; localized corrosion; XPS; AFM/SKPFM.

* Corresponding author: K.A. Yasakau, Department of Materials Engineering and Ceramic, CICECO, University of Aveiro, 3810-193 Aveiro, Portugal, Tel.: +351-234-401418; Fax: +351-234-378146; E-mail address: kyasakau@ua.pt

1 Introduction

Hot-dip galvanized steel is widely used as a structural material for various applications including complex shapes and structures like in car bodies. In the latter various metallic parts are traditionally joined by point welding or fastening. Recently the adhesive bonding is growing as an alternative joining technology especially in the case of multi-material structures. It offers important benefits such as good mechanical properties, additional stiffening effect, and reduction of galvanic corrosion between the joined parts [1]. However, de-adhesion or delamination of the adhesive joint may occur when exposed to a corrosive environment. De-adhesion is a consequence of the degradation of the polymer-metal interface [2]. The damaged interface may easily stay unnoticed due to the complexity and high cost of the techniques available for the inspection of adhesive joints. The consequences of the degradation of adhesive joints can be more structurally deleterious than the corrosion degradation of painted metals due to the loss of mechanical integrity of the joint.

Therefore it is important not only to ensure the high adhesion strength between the metal surface and an adhesive layer but also guarantee the durability of the joint under corrosive environment. The joint performance in terms of adhesion and durability relies heavily on the surface chemistry of metal substrates as well as the characteristics of the interface between an adhesive and the metal surface. Targeted pre-treatments on galvanizing coatings such as substrate cleaning or application of adhesion promoters may improve the adhesion strength to organic matrixes [3,4]. The surface properties of zinc galvanizing layers may also be modified during the galvanizing process [5].

In the hot-dip galvanization process a ferrous substrate is immersed in a bath of molten zinc or zinc alloy at around 450°C. During immersion the metal piece is covered by a layer of zinc with Fe-Zn phases closer to the interface. The formation of the latter can be inhibited by adding typically 0.1-0.3 wt.% of Al to the galvanizing bath. Iron diffusion to zinc is inhibited by Fe₂Al₅ intermetallic layer which improves the performance of the galvanized coating [6,7]. In the last decades various zinc coatings containing Al and Mg additions or other coatings based on Al alloys have been developed as promising substitutes to common zinc galvanizing coatings. Such coatings present better properties compared to conventional zinc hot-dip galvanizing ones [8-10]. Among these one can mention the superior corrosion protection in environmental corrosion tests. Such behaviour is obtained due to the specific microstructure of the alloys obtained during the galvanizing process. The operating parameters of the galvanizing process such as the bath temperature, dipping time, line speed can be optimized to control the efficiency of the zinc coating formation during the immersion step [11]. After the dipping process the thickness of the galvanizing coating can be controlled by the stripping (air knife wiping) process. In this process wiping dies remove an excess of liquid zinc metal from the surface with a gas stream. After the galvanization is complete the substrates are subjected to either cooling or additional heat treatment.

The composition of the gaseous mixture during the stripping or cooling processes may affect the surface oxide film chemistry and the microstructure of the galvanizing layer. Consequently, the different chemistry of the surface oxide films and zinc coatings microstructure may affect the adhesion properties and corrosion performance. Adhesion strength at metal - adhesive interface is mainly governed by the adsorption theory taking into account the intermolecular contact between atoms. This interaction can be produced through van der Waals, acid-base and covalent interactions [12]. The latter largely contribute to the adhesion strength due to the high energy of the formed bonds. In the adhesion process both substrate and adhesive chemistries including the hydroxyl content [13], functional groups and surface oxide thickness [14] are important.

The composition of the galvanizing bath mainly determines the coating microstructure [15]. However, air knife wiping, cooling process, bath temperature and the time of immersion can also affect the coating microstructure [16,17]. This in turn influences the susceptibility to corrosion and the localized corrosion behavior of the galvanized layer due to the existence of phases, which have higher activity than the zinc solid solution [18]. When a galvanized layer is covered by an adhesive (or organic coating) the localized corrosion process at adhesive – metal interface may largely contribute to de-adhesion process [19]. Therefore, the understanding of the local corrosion phenomena on zinc galvanizing coatings is required for prediction of a possible de-adhesion tendency in adhesive joints.

The knowledge of the factors affecting surface chemistry, microstructure and corrosion behaviour of zinc galvanizing coatings is important for improving the adhesion strength and inhibiting or delaying the de-adhesion during ageing in a corrosive environment. The aim of this work was to study the surface and electrochemical properties of steel galvanized with Zn and Zn-Mg-Al alloys prepared in a hot-dip galvanizing simulator. In particular the effects of stripping/cooling atmospheres on the surface chemical composition, the localized corrosion susceptibility and the adhesion strength to a model adhesive were investigated by means of spectroscopic, microstructural, electrochemical and mechanical techniques.

2 Experimental

2.1 Materials

Zinc galvanized samples were prepared in a hot-dip galvanizing simulator at Salzgitter Mannesmann Forschung GmbH. A 0.8 mm thick steel sheet of grade S320GD was used as substrate. Two galvanized coatings were produced: a common hot-dip layer with around 0.3 wt.% of aluminium (Z), and a coating containing around 1 – 2 wt % of Al and Mg (ZM). The thickness of the produced coatings was around 25 μm . The thickness was adjusted by a high pressure gas stream (stripping process) which blows excessive zinc off the galvanized surface. After this process the coated steel sheets were cooled at the same cooling rate. Ambient air and nitrogen (N_2) atmospheres were used in the stripping and cooling processes. Two extreme conditions were used: stripping – N_2 and cooling – N_2 (samples Z(N_2) and ZM(N_2)) and stripping – air and cooling – air (samples Z(air) and ZM(air)).

The galvanized samples prior to the studies were cleaned sequentially in Acetone, 2-propanol and absolute ethanol solvents in ultrasonic bath during 10 min in each step, then dried and stored in a desiccator.

Ultrapure Millipore™ water $>18 \text{ M}\Omega\cdot\text{cm}$ was used for preparation of 5 mM NaCl (99.5 wt.% purchased from Aldrich) solution having pH around 6.

2.2 Techniques

XPS: X-ray photoelectron spectroscopy was used to study the influence of stripping and cooling atmosphere treatments and ageing process on the surface chemistry of Z and ZM. X-ray photoelectron spectra were recorded with an Omicron ESCA+ System (Omicron NanoTechnology GmbH, Germany), utilizing a Al $K\alpha$ X-ray source and a spot diameter of 600 μm , with a step size of 0.05 eV at a constant pass energy of 25 eV and a base pressure of $< 2 \cdot 10^{-9}$ mbar. The take-off angle was set to 60° with respect to the surface plane. The spectra were fitted with the CASA XPS software using a Shirley background and a mixture of Gaussian and Lorentzian fitting for the peak shapes. For the quantification, relative

sensitivity factors supplied from Omicron GmbH were implemented in the CASA XPS database. All spectra were calibrated using the C1s peak (binding energy (BE) = 285 eV) as internal reference.

SEM/EDS. Scanning Electron Microscopy/Energy Dispersive Spectroscopy (SEM/EDS) studies of surface microstructure and elemental composition were performed by FEG SEM system Hitachi SU-70 with accelerating voltage 25 kV.

AFM/SKPFM. Atomic Force Microscope (AFM) Digital Instruments NanoScope III system with Extender™ Electronic Module was used for the acquisition of topography and Volta potential maps on the polished adhesive-zinc-steel cross-section and polished zinc plane surface. Topography was acquired in tapping mode when the tip was in intermittent contact with the substrate. For the Scanning Kelvin probe force microscopy (SKPFM) measurements AFM was operated in the interleave mode with two pass scans. The first pass acquired the topography of the surface. During the second scan the tip was lifted up from the surface by 100 nm and the ac voltage of 5 V was applied between the tip and the sample to induce oscillations of the cantilever. Using a nulling technique, the Volta potential difference between the sample and the tip was measured over the whole surface to obtain the map of the Volta potential difference (VPD). Topography and VPD maps with surface area 20 by 20 μm were obtained. For all SKPFM measurements, silicon probes covered with Cr/Pt layers were used. Measurements were performed at around 23 ± 1 °C and 55 ± 3 % RH. Volta potential values of metal substrates are presented versus standard hydrogen electrode (SHE). For that firstly VPD potential of a pure Ni surface was measured [20], then the VPD vs. Ni ref. was converted to SHE potential using the calibration data from [21].

SKP. A custom made height regulated scanning Kelvin probe was used to analyse the induced changes in the oxide chemistry of Z and ZM samples prepared under different stripping and cooling atmospheres. The experiments were performed under high humidity (>90 % RH) and the interface potentials were referenced to Cu/CuSO₄ electrode prior to the measurements. The Volta potential values were reported vs. Standard Hydrogen Electrode (SHE).

Electrochemical measurements. DC polarization measurements were performed using a Gamry potentiostat PCI4. A three-electrode cell consisting of a working electrode galvanized steel with an area of 1 cm², Pt spring counter electrode with surface area about 2 cm² and a reference saturated calomel electrode (SCE) combined with a Luggin capillary. The potential was scanned at a sweep rate of 1 mV/s in the range from -0.15 V to 0.30 V vs. open circuit potential (OCP). Prior to the DC polarisation measurements OCP data were collected for 30 minutes.

AFM in situ measurements. Pico LE AFM microscope was used for in-situ measurements of galvanized surfaces during immersion in 5 mM NaCl. The AFM was operating in AAC-mode (semi-contact mode). A preliminary topography was acquired in air to select a place for in-situ investigation. In-situ measurements were performed in a liquid cell consisting of an O-ring firmly pressed against a flat sample. The formed pool had a volume of around 0.6 ml. AFM measurements started after the electrolyte was injected in the liquid cell. AFM was operated in semi-contact mode in liquid, which allowed to minimize the tip-sample force. The resonance peak of the cantilever during the in-situ mode was around 120-150 kHz. The samples after measurements were rinsed with deionized water and then the water from the surface was carefully soaked by filter paper. In the end the samples were dried in a flow of warm air and stored in a desiccator.

Peel force setup. Metal samples of a size of 30x50 mm were cleaned according to the above mentioned cleaning procedure. The left and right hand sided areas of the sample (long side) were covered in about 0.5 cm with one layer of Magictape and two layers of Tesafilm above each other. An additive-

free epoxy-amine hot curing adhesive based on epoxy resin D.E.R 331 P (Dow Chemicals) and amine hardener (Jeffamine D400) was used as an adhesive and was applied to the metallic alloy substrate forming a polymeric film. The used adhesive (2.25 g DGEBA, 0.75 g DGEPEG, 1.02 g Jeffamine) was degassed for 2 h, applied upon the non-covered metal under nitrogen atmosphere (<10 % RH) and was dried for 30 min at room temperature and cured for 2 h at 130 °C. The samples before testing were kept during 1 day of exposure at 40 °C and RH > 95 %. The standalone films were tested on a 90° peel-test setup. The device consisted of two parts namely: a force gauge model ZP-5, Imada, Tokyo, Japan which was used to detect the peel force, and a motorized peel tester MV-220 Motorized Test Stand, Imada, Tokyo, Japan moving at a speed of 5 cm/min.

3 Results and discussion

3.1 Surface chemistry characterisation by XPS

The surface chemistry of the Z and ZM samples prepared under different stripping atmospheres was investigated by means of XPS analysis. The survey spectra of Z and ZM galvanizing coatings confirmed the presence of C, O, Zn, Al on the surface, whereas Mg was additionally found on ZM coatings. Figure 1 presents high resolution XPS spectra of C 1s O 1s, Zn 2p and Al 2p core level spectra acquired on Z(N₂) sample and Mg 2p for the ZM(N₂) sample as an example. The C 1s core level spectra can be fitted with three different contributions. The contribution at lower BE (binding energy) (≈284.5 eV) corresponds to C-C aliphatic species, whereas the contribution at 286 eV is assigned to C-O and C=O bonds. The contribution at higher BE (≈288.0 eV) is associated to COO⁻ species. The O1s core level group can be also fitted with three contributions. According to the literature, an excellent fitting was obtained with symmetric components of equal full width at half maximum separated by 1.2-1.4 eV. The contribution at lower BE (≈530.5 eV) corresponds to the oxide lattice of the coatings. The contribution at 531.8 eV is assigned to the presence of hydroxides on the surface coatings and the contribution at higher BE (≈533.2 eV) is associated to the formation of a carbonate ad-layer on top of the coatings. The Al 2p core level can be described as single or double doublets which may reflect two different oxidation states of the Al. Thus, the doublet located at 72.1 eV corresponds to metallic aluminium Al(0), whereas the doublet at higher BE (≈74.5 eV) is assigned to oxidized aluminium species Al(III). The Zn 2p^{3/2} core level can be also fitted with two different contributions which reflect different oxidation states. The contribution at lower BE (≈1020.8 eV) corresponds to metallic zinc Zn(0) whereas the main contribution at 1021.8 eV is assigned to oxidized zinc species Zn(II). The Mg 2p core level is fitted with only one contribution centred at 49.5 eV which is assigned to oxidized magnesium species Mg(II) [22].

Table 1 represents the metal ratio of the coatings prepared under different stripping conditions. The analysis of the metallic species distribution on the surface indicates that Z and ZM samples surface has high Al and Mg (only in case of ZM) concentration compared to Zn (Table 1). The XPS analysis of the Z samples prepared under air conditions, revealed an Al/Zn ratio of ~18, whereas this ratio is about 9 on Z(N₂) sample (Table 1). The higher Al/Zn ratio can be related to the preferential oxidation of aluminium in air and faster diffusion of Al to the surface, in contrast to the lower ratio that might be explained due to the suppression of Al diffusion to the surface during the solidification of the galvanizing coating in nitrogen atmosphere. The XPS analysis of the ZM samples prepared under different stripping conditions revealed a similar surface chemistry. The Al to Zn ratio of the ZM air sample is ~14 and is slightly raised up to 16 when manufactured in N₂ conditions. The Mg to Al ratio remains constant (~0.6) on both ZM surfaces. In the ZM specimens there is no significant enrichment or depletion of any elements during the solidification of the alloy. Preparation in nitrogen conditions reduces considerably the

amount of oxidized species on the surface resulting in thinner oxide passive films as follows from the higher ratio of metals to oxygen species.

Table 2 presents in more details the chemical species compositions on Z and ZM samples prepared under air and N₂ stripping and cooling atmospheres. It can be seen that the surface chemistry of Z and ZM samples and the nature of the passive layer were strongly influenced by the stripping atmosphere. For instance, the surface of the Z(air) specimen was covered by an Al-Zn-oxide layer which was partially hydroxylated (having OH⁻ groups). The Zn was detected as oxide and as metallic contribution as well (Table 2). Under N₂ conditions, due to the non-oxidative atmosphere during the alloy solidification, a significant amount of metallic Al was detected which suggests a thin oxide layer covering the galvanizing coating. Moreover the hydroxylation degree was also higher on Z(N₂) sample. In the case of ZM specimens prepared in air conditions, a mixture of hydrated carbonate ad-layer covered the outer surface as reflected by the higher content of CO₃²⁻ species. The ZM specimens prepared under N₂ conditions show a higher metallic contribution for Al and Zn, suggesting a thinning of the passive layer during the solidification of the alloy coating. On the surface of both ZM samples Mg seems to stay in the oxidized form. The passive layer on the surface of ZM(N₂) is higher hydroxylated than on the ZM(air). In general terms, the use of a non-oxidative atmosphere during the alloy solidification process results in the formation of a thinner oxide layer on the galvanizing coatings surface.

3.2 Surface characterisation by electron microscopy and EDS

Figure 2 presents SEM and EDS maps of Z samples prepared under air and nitrogen conditions. SEM images of both Z samples reveal the grain microstructure where intergranular zones were clearly visible (Figure 2a,d). Such clear grain structure was achieved in the course of solidification during the hot-dip galvanizing process. The grain size ranges from 20 to 100 μm in the case of the Z(air) sample. As revealed by the EDS mapping (Figure 2b,c) the grain boundaries contained a higher concentration of aluminium and oxygen compared to the bulk grain composition. The microstructure of Z(N₂) sample revealed a noticeable difference (Figure 2d). The grain structure is characterized by irregular long grains with the size ranging from 150 to 400 μm (Figure 2d). EDS mapping analysis of the surface did not reveal the defined segregation of Al and O at grain boundaries but an homogeneous distribution of these elements along the surface (Figure 2e,f).

In the galvanizing process zinc solid solution grains start to grow when temperature reaches 419°C [11]. The maximum solubility of Al in zinc (beta) phase is 1.2 wt.% at eutectic temperature (382°C). Al solubility decreases till 0.03 wt.% at room temperature. The segregation of Al and O in grain boundaries of Z(air) sample may be explained by excessive oxidation of Al in air atmosphere. During the cooling process aluminium oxide may segregate in grain boundaries zones due to lower miscibility with zinc matrix. On the other hand in nitrogen atmosphere such process does not occur and Al distributes more equally within the zinc matrix.

Figures 3 presents SEM and EDS maps of ZM samples surface prepared under air and nitrogen conditions. SEM micrographs acquired on ZM samples (Figure 3a,d) do not show well defined grain boundaries as in the case of Z samples. The surface of both ZM samples shows zinc solid solution rich islands about 10-20 μm in diameter (Figure 3a,d). ZM(N₂) surface shows more round and confined islands compared to ZM(air) ones. Zinc rich islands are surrounded by binary and ternary eutectic phases containing Al, Mg as can be distinguished from the EDS maps (Figure 3b,e). The distribution of Mg and Al looks similar on both ZM samples surfaces. The oxygen EDS maps show several regions with high oxygen concentration compared to the surrounding matrix. Such areas may have a thicker oxide film

(Figure 3c,f). The composition of the binary and ternary eutectic phases can be described by $MgZn_2$, Zn and Al phases as it can be deduced from the phase diagrams of Mg-Zn and Zn-Al equilibrium diagrams and XRD measurements (not shown) [11,23]. Mg_2Zn_{11} phase which can be found in Zn-Mg alloys [24] has not been found in ZM samples. In general the phase composition and microstructure of ZM(air/N₂) samples is similar to those found in other reports indicating $MgZn_2$, Zn and Al phases [25,26]. Moreover there is no defined influence of the atmosphere during the galvanizing process on the microstructure of the galvanizing coatings.

3.3 Surface characterisation by AFM, SKPFM and SKP

Surface analysis of Z and ZM samples by AFM/SKPFM is presented in Figure 4. AFM maps were acquired on the surface containing grain boundaries in order to locate possible heterogeneous properties of passive surface oxide film or changes in elemental distribution on the surface. SKPFM analysis of Z samples surface revealed high VPD on grain boundary zones (Figure 4 b,d). Bulk grains, however, show a more uniform distribution of Volta potential on the surface of both Z substrates. Such results agree with the microstructural and EDS analysis performed earlier (Figure 2). The accumulation of Al and O elements and other impurities in grain boundaries is reflected in well-defined VPD increase at Z(air) sample grain boundaries (Figure 4b). VPD analysis of Z(N₂) sample also shows the increase of VPD at the grain boundaries (Figure 4d). The maximum VPD difference between grain boundaries and matrix can reach values up to 160 mV and 90 mV on Z(N₂) and Z(air) samples respectively. Although the Al accumulation has been preferentially found on Z(air) samples, the VPD increase may be also affected not only by Al and O but by impurities segregation as well. The average level of VPD on Z(air) surface is -0.63 V which is higher compared to VPD level on Z(N₂) sample i.e. -0.85 V (Table 3).

In contrast to Z samples, VPD distribution on ZM samples is different. First of all the grain boundaries between zinc solid solution and eutectic phases are not clearly defined on the topographical maps (Figure 4e,g). Moreover, there was no clear distinction between the zinc solid solution regions and eutectic phases on SKPFM images (Figure 4f,h). VPD maps show different zones with high (bright zones) and low (darker zones) Volta potential on the surface (Figure 4f,h). Such places may have different surface oxide composition and distribution of Zn, Al and Mg elements on the surface. The areas with lower VPD could be attributed to regions with contribution from Mg containing phases, while the zones with higher VPD could be ascribed to the places where the oxide film is thicker. The high heterogeneity of the surface is also reflected in average VPD values of ZM(air) and ZM(N₂) samples which are -1.11 V and -0.76 V respectively (Table 3).

Complementary to the SKPFM experiments, SKP measurements were performed on Z and ZM substrates prepared under different stripping conditions. Figure 5 shows the SKP line scans for all systems. The Z specimens prepared under air atmosphere reveals a higher VPD (-0.77 V) than the Z specimens prepared under N₂ atmosphere (-0.89 V) (Table 3). SKP line profiles indicate quite a homogeneous potential distribution and thus the surface oxide composition on Z samples. Differences in the VPD within the grain boundaries could not be resolved due to the limited lateral resolution of the SKP technique. The Kelvin Probe potentials values found for both ZM(air) and ZM(N₂) were around -1.26 V and -1.16 V respectively, which is significantly lower than for the Z specimens. Such trend is attributed to the presence of Mg oxide within the surface. In addition both scan lines yield high deviation of Volta potential values which differ up to 200 mV along the whole scan, pointing towards the heterogeneity of the surface regarding the oxide chemistry. As observed by means of the SEM the distribution of the

different elements on the surface of the Z specimens were more homogenous than for the ZM specimens where eutectic phases and Zn-rich islands were found.

As seen in the listed VPD values in Table 3, despite the different scale resolution, the results obtained by means of both techniques correlate quite well. The main changes in the Volta potential can be ascribed to variations of the surface chemistry of metals. Among the factors which may affect the VPD one can name the following: oxide thickness and nature, corrosion products films, oxide films from high temperature oxidation, water adsorption and different amount of hydroxyls groups [27-29]. The differences in the VPD for the Z samples prepared under air and nitrogen conditions can be explained in terms of a thinner oxide for the Z(N₂) sample (Table 2). Besides, the oxidation of the metal surface at high temperature often results in increase of the Volta potential of the surface due to charge injection into the oxide film [28]. The more negative values found for the ZM samples are consistent with the presence of Mg oxide. The latter has been identified by XPS analysis on ZM samples (Table 2). VPD is shifted accordingly to cathodic direction due to different electronic properties of MgO compared to ZnO [30]. The decrease of VPD to more cathodic potentials was clearly shown by Prosek et al. [31]. It was shown that the surface SKP potential progressively drops in humid air from -0.55 V vs. SHE on pure zinc surface to around -0.9 V vs. SHE on Zn4Mg alloy surface which was covered by MgO [31]. ZM(N₂), despite the thinner oxide film, shows a higher Volta potential (Table 3). This deviation can be explained by the higher density of hydroxyl groups which may increase the VPD on the surface as was reported by Ozkanat et al. [29]. In addition the differences regarding the hydroxides and carbonate groups concentration (Table 2) may have an impact on the deviation of the VPD found.

Chemical and electronic properties of the galvanizing surface depend on the atmosphere in which the coatings were produced. The main changes between the samples were attributed to the different hydroxylation degree, metallic to oxide ratio and presence of various oxides on the surface. Also the different chemical composition was correlated with Volta potentials of Z and ZM samples. It is interesting that the Volta potential of Z(air) was higher than Z(N₂), however the trend was opposite for ZM(air) and ZM(N₂) samples. The chemical composition of the surface oxide films is expected to impact the adhesive properties of the galvanizing coatings to model adhesive films.

3.4. Adhesive properties

In order to get a better understanding of the adhesive properties of the Z and ZM specimens 90° peel test experiments have been performed. Before testing, samples were aged for 24 h at a temperature of 40 °C and RH > 90 %. Figure 6 shows the peel force of the Z and ZM specimens prepared under different stripping and cooling atmospheres. The Z(air) and ZM(air) surfaces yield a peel force value around 0.1 N/mm. The Z(N₂) surface yields a value around 0.25 N/mm, whereas the ZM(N₂) yields a peel force 0.75 N/mm. In general, the samples processed under nitrogen atmosphere show higher peel force when compared to the samples processed under air atmosphere.

In order to understand these results, the Z and ZM samples were exposed to similar aging conditions as the specimens coated with the adhesive. Table 4 summarizes the elemental composition and different species ratio for the Z and ZM samples prepared under different stripping conditions after the ageing process. The aging process in humid atmosphere leads to the oxidation process of metallic surface. Indeed the XPS spectra acquired after the aging demonstrate an increase of oxygen species and a total depletion of metallic species on the metal surface (Tables 2 and 4). In particular, Z(N₂) and ZM(N₂) samples demonstrated a higher growth of oxide species (O_x) on the surface after the aging process compared to air treated samples (Table 4). Initially the samples prepared in nitrogen atmosphere have a

lower oxide film thickness and a higher metallic content. During the ageing process metal is converted to oxides/hydroxides. The hydration of the oxide layer during the aging is detrimental because the resulting metal-hydrates generally exhibit very poor adhesion to their base metals [32].

The adhesion strength of the adhesive film to the surfaces is mainly driven by the formation of strong chemical bonds between the adhesive and the surface. As observed by Valtiner, the direct formation of coordinative bonds between carboxylic groups and Zn metallic atoms resulted in increase of the adhesion force [33]. In the case of the fully hydroxylated surface, the binding via hydrogen bond is most dominant. However, under humid or corrosive condition, the coordinative bonds are much more stable than the ones based on hydrogen bonds [34]. In addition the formation of a carbonate ad-layer (CO_3^{2-}) on the surface may be deleterious for the adhesion performance between epoxy and metal surface. Thus, the surface chemistry of the coatings plays a major role on the adhesive strength. As discussed previously, the processing under nitrogen lead to a higher M^0/M^{n+} ratio and consequently thinner oxide film on the alloy surface as well as differences in the hydroxide/carbonate growth on the surfaces. Thus, the formation of coordinative bonds between the epoxy functionality and the rich metallic interface of the coatings prepared under N_2 atmospheres is likely, leading to an enhancement of the adhesion strength. In the case of the coatings prepared under air atmosphere, the surface chemistry of the alloys results in the development of a thick and fully hydroxylated surface which has a negative impact on the adhesion of the epoxy adhesive.

It needs to be stressed that the obtained results may not be completely valid for industrial applications. Firstly, the storage conditions of galvanized steel in industry are different. Secondly, before adhesive joining a pre-treatment or a conversion layer is applied onto a galvanized surface. Such procedures may change the surface properties of the galvanizing coatings and adhesion towards organic layers. Hence, the observed difference between the samples produced at different stripping atmosphere can vanish. Therefore, the subject studied in this paper presents an interest primarily for academic research.

3.5. Electrochemical studies

Figure 7 presents OCP and DC polarisation measurements on Z and ZM galvanized samples immersed in 5 mM NaCl solution. OCP evolution shows minimal difference between Z and ZM samples (Figure 7a). ZM samples presented a lower potential (≈ 20 mV) during the first 2 hours of immersion than Z samples. The lower OCP value is also reflected in the DC polarisation curves where the corrosion potential obtained for the ZM samples is lower than that of Z one (Figure 7b). A similar trend was also observed for the measurements conducted in 0.05 M and 0.5 M NaCl solutions (data not shown). As reported by Hausrand et al., the MgZn_2 phase has lower OCP with respect to pure Zn solid solution [35]. Therefore the lower potential of ZM sample can be associated with the presence of Mg rich phases on the alloy surface. At longer immersion the OCP evolution shows a slight increase of ZM potential and decrease of Z samples potential. The difference between OCP of both systems is small about 10-20 mV. Such difference could be caused by preferential corrosion of Aluminium and Magnesium containing phases and enrichment of the surface by corrosion products.

The DC polarisation curves were recorded after 30 min during which the corrosion potential was stabilized. Polarisation measurements present the initial corrosion activity of the zinc alloys. The used time is consistent with the time frame of in-situ studies. DC polarisation curves show significant difference in corrosion activity between Z and ZM samples. The cathodic portion of the curves shows the higher rate of oxygen reduction process on both Z samples compared to ZM ones (Figure 7b). Prosek et

al. also reported lower cathodic currents on Zn-Al-Mg alloys [35,36]. Most likely the difference is related to the surface coverage by different oxides. It is known that ZnO has semiconducting properties and a lower band gap than MgO [37]. The higher band gap energy might reduce electron transfer from the semiconductor to adsorbed oxygen species therefore reducing the kinetics of the oxygen reduction process [30,38]. In both cases we see a diffusion plateau of oxygen reduction and the difference in diffusion currents can be related to more difficult diffusion of oxygen towards the metal surface because of the oxide film on ZM samples. Anodic polarisation curves of Z samples did not show the formation of a passive region. ZM samples revealed a small though noticeable current increase at around -0.86 V (Figure 7b) which may be associated with the development of pitting corrosion. This potential is more positive than the pitting potential reported for MgZn₂ phase [39]. Therefore it can represent the pitting potential of the zinc matrix. In general, Z samples show higher electrochemical activity and have several times higher currents compared to ZM ones. However, it seems that the stripping and cooling atmospheres do not significantly affect corrosion of Z and ZM alloys at early stages of immersion.

3.6. Localized corrosion

Localized corrosion susceptibility of Z substrates was investigated by AFM in situ during immersion in 5 mM NaCl solution. A metal surface containing grain boundaries and bulk grains was selected for the analysis given the fact that grain boundaries have higher VPD than the base Z alloy matrix level. The high VPD difference between impurities and metal matrix may create local galvanic coupling and promote local corrosion attack [20]. Thus studying the corrosion behaviour of an area containing different electrochemically active regions is important for understanding the local corrosion phenomena.

Both Z(air) and Z(N₂) samples have demonstrated similar patterns which involve the localized corrosion at grain boundaries as the starting point on both substrates. Two different examples of localized attack are presented herein. Figure 8 presents AFM topography maps acquired on Z(air) sample at a zone containing grain boundary before immersion and during immersion in 5 mM NaCl solution. The metal surface started to dissolve immediately after immersion in the electrolyte. It can be seen that the grain boundary was subjected to localized corrosion attack which expanded to the surrounding metal matrix during the longer immersion time (Figure 8b,c). The optical image of the surface taken after 15 min immersion revealed a number of dark areas highlighted by contour lines (Figure 8d). These dark areas are mostly located on grain boundaries zones which preferentially dissolve during immersion. It confirms that the corrosion starts at grain boundaries and then spreads along the grain boundaries and to bulk grains at longer immersion time (not shown).

Similar to Z(air) the localized corrosion at grain boundary has been found on Z(N₂) sample. In addition to the localized attack, grain boundary zones have demonstrated a different behaviour. Figure 9 presents AFM topography maps acquired on a grain boundary of Z(N₂) sample before immersion and during immersion. As observed in Figure 9 after a short immersion time corrosion products appear on the grain boundaries of the Z(N₂) sample (Figure 9b). Similar to what has been found earlier optical image acquired during initial immersion showed well visible black regions residing at grain boundaries (Figure 9d). Black areas correlate with corrosion sites preferably subjected to anodic dissolution. The corrosion zones spread to the surrounding zinc solid solution zones. At longer immersion time all the surface was corroded (Figure 9c).

Localized activity of both ZM samples is different compared to Z ones. Figure 10 presents AFM topography maps acquired on the surface of ZM(air) sample before immersion and during immersion in

NaCl solution. The initial AFM map presents an area which is preferentially occupied by ternary and binary eutectic phases (Figure 10a). During immersion the surface was quickly covered with small corrosion precipitates having the height up to 250 nm (Figure 10b). RMS roughness of the surface increased from 26 nm to around 70 nm after the first 12 min of immersion. Such corrosion products are most probably formed as a result of fast corrosion process involving Al and MgZn₂ phases [18,40,41]. Initially bright zinc galvanizing coating develops a dark shade which is shown on the optical image (Figure 10d). The dark aspect suggests that the metal surface has been subjected to corrosion. During the first hour of immersion the topography did not show deep localized attack (not shown). The surface topography map after approximately 2 hours of immersion revealed a uniform corrosion products layer consisting of round shaped corrosion precipitates (Figure 10c). Both ZM(air) and ZM(N₂) samples during immersion develop a surface corrosion film unlike the Z samples that show a significant localized corrosion attack (Figures 8,9).

Although ZM samples do not have well distinguished grain boundaries a local corrosion attack also occurs on eutectic phases. Figure 11 presents AFM topography maps and optical image acquired on ZM(N₂) sample during immersion. The metal surface contains binary eutectic phase (#1) in the middle surrounded by ternary eutectic phases (#2) as highlighted on the topography map (Figure 11a). Optical image acquired after 20 min of immersion reveals several black areas which may be correlated with the development of corrosion activity and precipitation of corrosion products (Figure 11d). After 40 min of immersion, a pitting corrosion was detected over the surface indicated by arrows (Figure 11b). After an additional hour of immersion a clear dissolution zone has developed in the place of eutectic phases (Figure 11c). In situ AFM experiments show that local corrosion attack may develop on MgZn₂ eutectic phases during immersion. Since the electrochemical activity of MgZn₂ phase is higher [35] than the Zn solid solution it can be expected that the phase will be subjected to localized corrosion during immersion.

Local in-situ measurements contribute with the important information on the location of the first corrosive attacks on Z and ZM substrates. Both air and N₂ treated samples demonstrate similar behaviour suggesting that the atmosphere during galvanizing process does not significantly affect the samples localized corrosion. It has been shown that grain boundaries on Z sample are weak spots for the initial local corrosion initiation. Moreover corrosion product precipitates may selectively deposit on the grain boundaries. This behaviour is perfectly correlated with the SKPFM measurements presented earlier which show a higher VPD on grain boundaries zones. VPD maps predicted possible localized corrosion susceptibility of grain boundaries and localized in situ measurements allowed to observe their attack. ZM samples showed local corrosion damage which was mainly originated on MgZn₂ phases. However, the localized attack and surface corrosion on ZM sample in general seems to be less aggressive compared to Z one.

3.7. Microstructural analysis of samples after immersion in NaCl solution

Since the samples prepared under air and nitrogen atmospheres demonstrate similar degradation behavior, an in-depth microstructural analysis of only Z(air) and ZM(air) surfaces after corrosion has been performed. Figure 12 shows SEM micrograph and EDS elemental maps and spectra acquired on Z(air) sample surface. The zone where in-situ AFM measurements were performed earlier (Figure 8) is highlighted on SEM micrograph (Figure 12a). After immersion the surface is extensively corroded. Grain boundaries reveal a significant corrosion, and the surrounding zinc grains show visible dissolution. EDS maps show Al, Zn, Fe, O and Cl signals after corrosion (Figure 12b,d,e,f). The increase of Al content may be explained by preferential dissolution of a more active element (Zn) from the solid solution and

accumulation of aluminum corrosion products on the surface [41]. EDS analysis can acquire the characteristic X-ray signals of elements from a depth about several micrometers depending on the electron beam energy. When a zinc coating becomes thinner due to dissolution, electrons penetrate deeper and EDS may detect the signals from Al_5Fe_2 intermetallic barrier layer located at the iron-zinc interface. This may also explain the higher Al content. A significant dissolution of galvanized layer unveils steel substrate which explains Fe peak detected by EDS analysis (Figure 12f). The presence of oxygen and chlorine on the spectra clearly indicates a corrosion products film formed on the surface. Similar results were observed in the Z(N₂) sample after immersion (data not shown).

The corrosion induced damage of ZM samples is different compared to the Z samples surface. Figure 13 shows SEM micrograph and EDS elemental maps and spectra acquired on ZM(air) sample (as an example) after immersion. The square area on Figure 13a corresponds to a zone where in situ AFM measurements were performed. SEM micrograph shows round bright areas corresponding to zinc solid solution islands surrounded by eutectic phases (dark places) (Figure 13a). Despite visible corrosion attack, the main microstructural features of the galvanizing coating were still visible. However, both eutectic zones and Zn-rich islands were corroded. The characteristic features of ZM samples corrosion are a noticeable increase of aluminum signal (Figure 13b,f) and depletion of Mg (Figure 13e,f). $MgZn_2$ containing eutectic phases dissolve during immersion which explains the changes in Mg content. EDS spectra indicate a growth of oxygen and chlorine signals after immersion which is associated with the presence of corrosion products (Figure 13d,f). In addition, Fe signal was not detected by EDS analysis revealing a lower dissolution rate of ZM samples compared to Z ones.

The above results show that Z galvanized coatings demonstrate a higher corrosion damage compared to ZM ones. The zinc galvanized coatings of Z samples are subjected to severe localized attack which proceeds down to the steel substrate. Whereas the ZM samples show a more general dissolution which stops at some point most probably due to the formation of a dense corrosion products film. This film is enriched in Al as was found out by EDS analysis (Figure 13b,f). In literature the formation of corrosion products films enriched in Al is attributed to enhanced corrosion resistance of ZM galvanizing coatings [26].

4. Summary and conclusions

This study revealed the important influence of stripping and cooling atmospheres during the hot-dip galvanizing process on surface properties, microstructure, adhesion and localized corrosion of Zinc galvanized (Z) and Zn-Al-Mg galvanized (ZM) steel substrates.

Air and nitrogen atmospheres affect surface composition and microstructure. Z(air) surface shows smaller grains and non-uniform distribution of aluminium/oxygen, which is located preferably in grain boundaries. These have a significant more positive Volta potential difference with respect to the bulk zinc grains. Z(N₂) sample has bigger grains and a more uniform aluminium and oxygen distribution in the metallic matrix. Though, grain boundaries zones in Z(N₂) also show high Volta potential difference between the grain boundaries and bulk matrix. VPD level on Z(air) sample is higher than on Z(N₂) one. This difference has been attributed to a thicker oxide film on Z(air) surface versus Z(N₂) one and effect of high temperature oxidation.

Air and nitrogen atmospheres do not produce any significant change on the microstructure of ZM coatings unlike for Z ones. However, SKPFM and SKP measurements clearly show that ZM(air) sample has lower VPD level than ZM(N₂). This tendency is opposite to what was observed with Z samples. The

lower VPD potential of ZM(air) surface can be explained by the presence of MgO which shifts VPD to the cathodic direction. Oppositely, ZM(N₂) sample has a higher VPD which can be associated to the contribution from the higher density of OH groups on its surface.

Peel test studies have showed an improved adhesion of ZM(N₂) to adhesive and a slight increase in adhesion on Z(N₂) samples in comparison to the respective air-treated samples. The increase in adhesive strength has been attributed to a thinner oxide film and to the presence of hydroxyl groups on the surface. Overall, the results demonstrate that the processing conditions and surface composition play a major role in improving the adhesion between a galvanized surface and an epoxy-amine based adhesive. It is suggested that the galvanizing process involving nitrogen atmosphere is better for adhesion strength between the galvanizing coatings and the organic adhesive layer.

It has been shown that the atmosphere does not affect general corrosion activity of Z and ZM alloys. Both Z samples show higher cathodic activity and corrosion rate than ZM samples as was demonstrated by DC polarisation.

The stripping atmospheres did not significantly affect localized corrosion of Z and ZM samples. Both Z samples demonstrate preferential corrosion attack initiated at grain boundaries. The possibility of such behavior has been suggested by the SKPFM analysis indicating a substantial VPD difference in such zones. Unlike for Z coatings, ZM coatings demonstrate a more homogeneous attack. However there is a clear evidence that binary eutectic (MgZn₂ phase) may exhibit the preferential dissolution. Moreover, ZM samples surface shows the depletion of Mg and growth of Al signals, suggesting the preferential Mg and Zn dissolution. Judging by the microstructural and elemental analysis after short immersion tests ZM samples present the enhanced resistance to local attacks on metallic matrix compared to Z samples.

Acknowledgements

K. Yasakau thanks the Portuguese Foundation for Science and Technology (FCT) and “Programa Operacional Capital Humano, participado pelo Fundo Social Europeu e por fundos nacionais do MCTES” for the financial support in form of a Post-Doctoral grant (ref. SFRH/BPD/80754/2011). The financial support of Research Fund for Coal and Steel within the DURADH “Durability of adhesively bonded surfaces finished galvanized steels in corrosive environments” project (ref. no. RFSR-CT-2011-00019) is gratefully acknowledged.

References

1. L.L. Shreir, R.A. Jarman and G.T. Burstein, Corrosion, Vol. 1, 3rd edn, Butterworth-Heinemann, Oxford, 1994.
2. W. Furbeth, M. Stratmann, The delamination of polymeric coatings from electrogalvanised steel – a mechanistic approach: Part 1: delamination from a defect with intact zinc layer, Corros. Sci. 43 (2001) 207-227.
3. P. Puomi and H. M. Fagerholm, Characterization of hot-dip galvanized (HDG) steel treated with bis-1,2-(triethoxysilyl)ethane and γ -aminopropyltriethoxysilane, J. Adhesion Sci. Technol. 15 (2001) 869-888.
4. P. Thissen, J. Wielant, M. Köyer, S. Toews, G. Grundmeier, Formation and stability of organophosphonic acid monolayers on ZnAl alloy coatings, Surf. Coat. Technol. 204 (2010) 3578–3584.
5. Hot-dip coatings, ASTM Handbook Corrosion, Vol. 13 (1999).

6. P. Biele, Determination of the active Al and Fe contents in the zinc bath and their influence on alloys-layer formation in the hot galvanizing process, in: *Galvatech'95* (1995) 769–776.
7. Y. De Abreu, A. Da Silva, A. Ruiz, R. Requiz, N. Angulo, R. Alanis, Study of zinc coatings on steel substrate attained by two different techniques, *Surf. Coat. Technol.* 120–121 (1999) 682–686.
8. B. Schuhmacher, C. Schwerdt, U. Seyfert, O. Zimmer, *Surf. Coat. Technol.* 163–164 (2003) 703–709.
9. T. Tsujimura, A. Komatsu, A. Andoh, in: *Proc. Galvatech June 2001, Belgium: Stahleisen, 2001*, pp. 145–152.
10. N.C. Hosking, M.A. Strom, P.H. Shipway, C.D. Rudd, Corrosion resistance of zinc–magnesium coated steel, *Corros. Sci.* 49 (2007) 3669–3695.
11. A.R. Marder, The metallurgy of zinc-coated steel, *Progress in Materials Science* 45 (2000) 191–271.
12. S.R. Hartshorn, *Structural adhesives*, Plenum Press, New York, 1986.
13. J. van den Brand, P. C. Snijders, W. G. Sloof, H. Terry, J. H. W. de Wit, Acid-Base Characterization of Aluminum Oxide Surfaces with XPS, *J. Phys. Chem. B* 108 (2004) 6017.
14. S. Maeda, Surface chemistry of galvanized steel sheets relevant to adhesion performance, *Prog. Org. Coat.* 28 (1996) 227–238.
15. C.E. Jordan, A.K. Marder, Interfacial layer development in hot-dip galvanneal coating in interstitial free (IF) steel, *Metall. Mater. Trans.* 25a (1994) 2101–2109.
16. C.E. Jordan, A.R. Marder, Alloy layer growth during hot-dip initial reaction of the Fe–Al layer during the first stages galvanizing at 450°C, in: *Galvatech '95* (1995) 319–325.
17. J. Davene, L. Dondin, J.K. Kem, S.I. Kin, Dynamic air knife: DAK, in: *Galvatech '95* (1989) 205–213.
18. J. Duchoslav, M. Arndt, R. Steinberger, T. Keppert, G. Luckeneder, K.H. Stellnberger, J. Hagler, C.K. Riener, G. Angeli, D. Stifter, Nanoscopic view on the initial stages of corrosion of hot-dip galvanized Zn–Mg–Al coatings, *Corros. Sci.* 83 (2014) 327–334.
19. A. Nazarov, M.-G. Olivier, D. Thierry, SKP and FT-IR microscopy study of the paint corrosion de-adhesion from the surface of galvanized steel, *Prog. Org. Coat.* 74 (2012) 356–364.
20. P. Schmutz, G.S. Frankel, Characterization of AA2024-T3 by Scanning Kelvin Probe Force Microscopy *J. Electrochem. Soc.* 145 (1998) 2285–2295.
21. A.B. Cook, Z. Barrett, S.B. Lyon, H.N. McMurray, J. Walton, G. Williams, Calibration of the scanning Kelvin probe force microscope under controlled environmental conditions, *Electrochim. Acta* 66 (2012) 100–105.
22. J. Duchoslav, R. Steinberger, M. Arndt, T. Keppert, G. Luckeneder, K.H. Stellnberger, J. Hagler, G. Angeli, C.K. Riener, D. Stifter, Evolution of the surface chemistry of hot-dip galvanized Zn–Mg–Al and Zn coatings on steel during short term exposure to sodium chloride containing environments, *Corros. Sci.* 91 (2015) 311–320.
23. P. Ghosh, M. Mezbahul-Islam, M. Medraj, Critical assessment and thermodynamic modeling of Mg–Zn, Mg–Sn, Sn–Zn and Mg–Sn–Zn systems, *Calphad*, 36 (2012) 28–43.
24. K. Honda, W. Yamada and K. Ushioda, Solidification Structure of the Coating Layer on Hot-Dip Zn-11%Al-3%Mg-0.2%Si-Coated Steel Sheet, *Materials Transactions* 49 (2008) 1395–1400.
25. M. Vlot, M. Zuijderwijk, M. Toose, L. Elliott, R. Bleeker, T. Maalman in, *Proceedings Galvatech 2007, ISIJ*, 510–515.
26. S. Schuerz, M. Fleischanderl, G.H. Luckeneder, K. Preis, T. Haunschmied, G. Mori, A.C. Kneissl, Corrosion behaviour of Zn–Al–Mg coated steel sheet in sodium chloride-containing environment, *Corros. Sci.* 51 (2009) 2355–2363.

27. A. Nazarov, D. Thierry, Probing the atmospheric corrosion of metals: zinc, *Prot. Met.* 42 (2006) 437–451.
28. K.A. Yasakau, A.N. Salak, M.L. Zheludkevich and M.G.S. Ferreira, Volta Potential of Oxidized Aluminum Studied by Scanning Kelvin Probe Force Microscopy, *J. Phys. Chem. C* 114 (2010) 8474–8484.
29. O. Ozkanat, B. Salgin, M. Rohwerder, J. M. C. Mol, J. H. W. de Wit, and H. Terryn, Scanning Kelvin Probe Study of (Oxyhydr)oxide Surface of Aluminum Alloy, *J. Phys. Chem. C* 116 (2012) 1805–1811.
30. R. Hausbrand, M. Stratmann, M. Rohwerder, The Physical Meaning of Electrode Potentials at Metal Surfaces and Polymer/Metal Interfaces: Consequences for Delamination *J. Electrochem. Soc.* 155 (7) (2008) C369–C379.
31. T. Prosek, A. Nazarov, U. Bexell, D. Thierry, J. Serak, Corrosion mechanism of model zinc–magnesium alloys in atmospheric conditions, *Corros. Sci.* 50 (2008) 2216–2231.
32. K. Dušek Ed., Epoxy Resins and Composites II, in *Advances in Polymer Science*, (1986), pp. 33-71.
33. C. Kunze, M. Valtiner, R. Michels, K. Huber, G. Grundmeier, Self-localization of polyacrylic acid molecules on polar ZnO(0001)-Zn surfaces, *Phys Chem Chem Phys.* 27 (2011) 12959-12967.
34. M. Maxisch, P. Thissen, M. Giza, G. Grundmeier, Interface chemistry and molecular interactions of phosphonic acid self-assembled monolayers on oxyhydroxide-covered aluminum in humid environments, *Langmuir* 27 (2011) 6042-6048.
35. R. Hausbrand, M. Rohwerder, M. Stratmann, C. Schwerdt, B. Schuhmacher, G. Grundmeier, in: *Proc. Galvatech* June, 2001, pp. 161–167.
36. M. Salgueiro Azevedo, C. Allély, K. Ogle, P. Volovitch, Corrosion mechanisms of Zn(Mg,Al) coated steel: 2. The effect of Mg and Al alloying on the formation and properties of corrosion products in different electrolytes *Corros. Sci.* 90 (2015) 482–490.
37. J.-H. Huang, C.-P. Liu, The influence of magnesium and hydrogen introduction in sputtered zinc oxide thin films, *Thin Solid Films* 498 (2006) 152–157.
38. R. Hausbrand, M. Stratmann, M. Rohwerder, Delamination resistant zinc alloys: simple concept and results on the system zinc–magnesium, *Steel Res. Int.* 74 (2003) 453–458.
39. R. Hausbrand, M. Stratmann, M. Rohwerder, Corrosion of zinc–magnesium coatings: Mechanism of paint delamination, *Corros. Sci.* 51 (2009) 2107–2114.
40. J. Sullivan, S. Mehraban, J. Elvin, In situ monitoring of the microstructural corrosion mechanisms of zinc–magnesium–aluminium alloys using time lapse microscopy, *Corros. Sci.* 53 (2011) 2208–2215.
41. P. Volovitch, T.N. Vu, C. Allély, A. Abdel Aal, K. Ogle, Understanding corrosion via corrosion product characterization: II. Role of alloying elements in improving the corrosion resistance of Zn–Al–Mg coatings on steel, *Corros. Sci.* 53 (2011) 2437–2445.

Figure captions

Figure 1. High resolution elemental spectra of a) C 1s, b) O 1s, c) Zn 2p and d) Al 2p of the Z(N₂) sample and e) Mg 2p of the ZM(N₂) sample.

Figure 2. SEM micrographs and EDS maps of Al and O elements acquired on Z(air) (a,b,c) and Z(N₂) (d,e,f) sample surfaces.

Figure 3. SEM micrographs and EDS maps of Al/Mg and O elements acquired on ZM(air) (a,b,c) and ZM(N₂) (d,e,f) samples surface.

Figure 4. AFM (a,c,e,g) and SKPFM maps (b,d,f,h) of Z(air), (a, b), Z(N₂) (c, d), ZM(air) (e, f) and ZM(N₂) (g, h).

Figure 5. Scanning Kelvin Probe potentials of Z and ZM specimens prepared under air and N₂ atmospheres.

Figure 6. Peel forces measured on different substrates coated with adhesive layers.

Figure 7. OCP evolution (a) during immersion in 5 mM NaCl solution; representative DC polarisation curves (b) acquired on Z and ZM samples after 0.5 h immersion in 5 mM NaCl solution.

Figure 8. AFM maps (a,b,c) and surface optical picture (d) obtained on Z(air) sample during immersion in 5 mM NaCl.

Figure 9. AFM maps (a,b,c) and surface optical picture (d) obtained on Z(N₂) sample during immersion in 5 mM NaCl.

Figure 10. AFM maps (a,b,c) and surface optical picture (d) obtained on ZM(air) sample during immersion in 5 mM NaCl.

Figure 11. AFM maps (a,b,c) and surface optical picture (d) obtained on ZM(N₂) sample during immersion in 5 mM NaCl.

Figure 12. SEM and EDS analysis of Z(air) sample surface after 2h corrosion. The square corresponds to the area presented in Figure 8.

Figure 13. SEM and EDS analysis of ZM(air) sample surface after 2h corrosion. The square corresponds to an area presented in Figure 10.

Figures

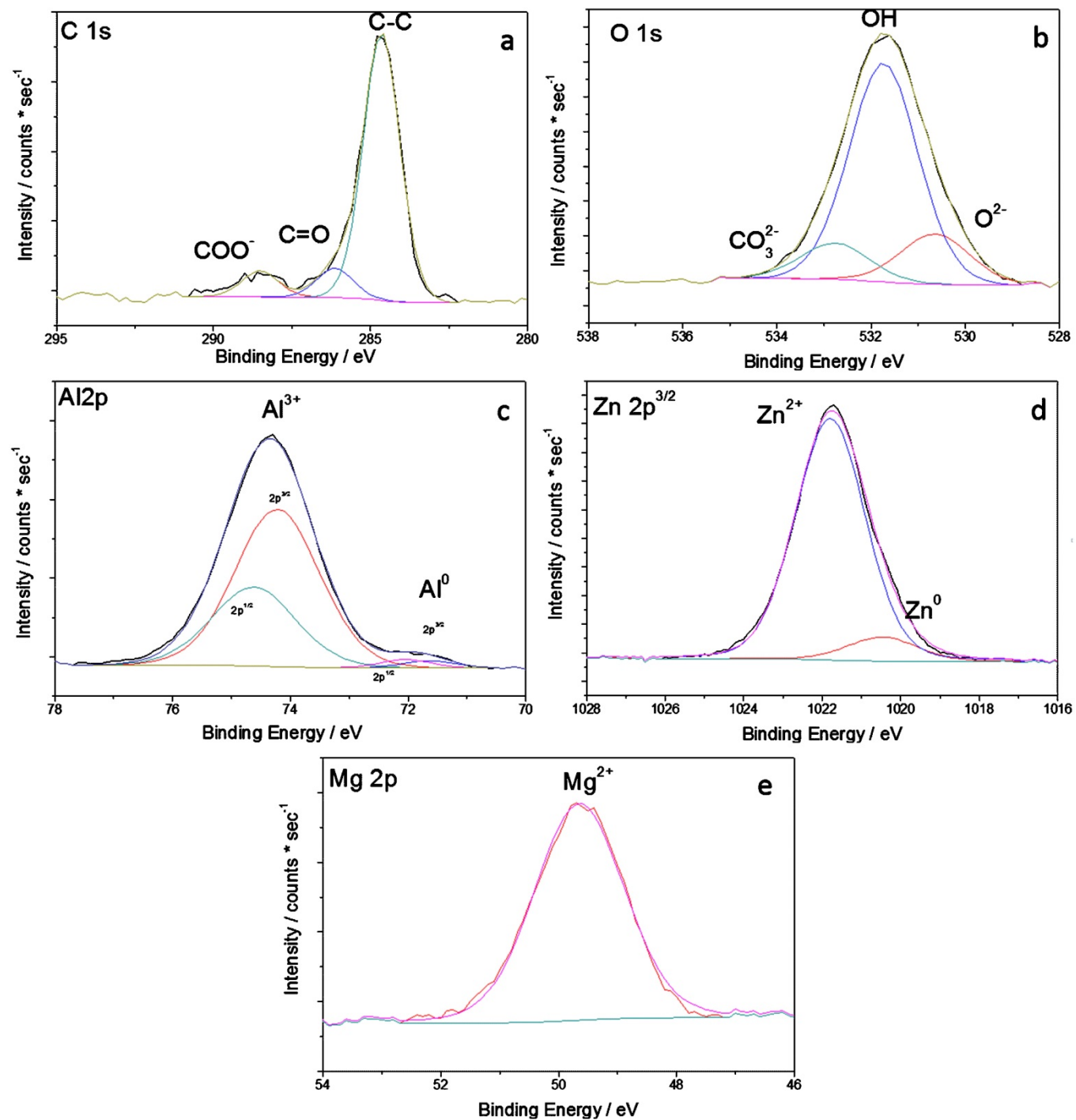


Figure 1. High resolution elemental spectra of a) C 1s, b) O 1s, c) Zn 2p and d) Al 2p of the Z(N2) sample and e) Mg 2p of the ZM(N2) sample.

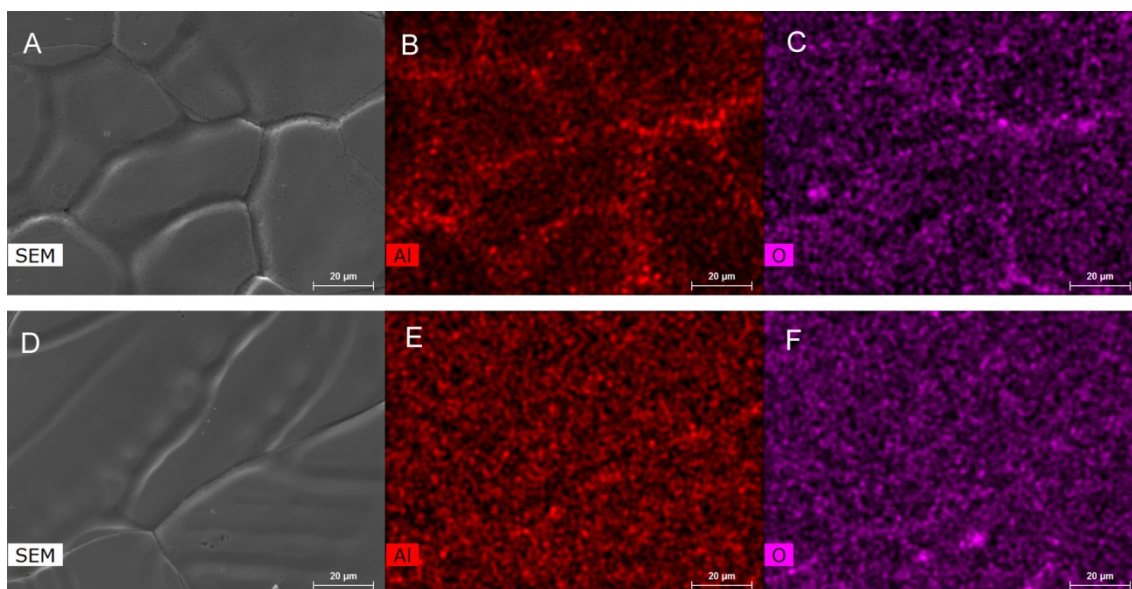


Figure 2. SEM micrographs and EDS maps of Al and O elements acquired on Z(air) (a,b,c) and Z(N₂) (d,e,f) sample surfaces.

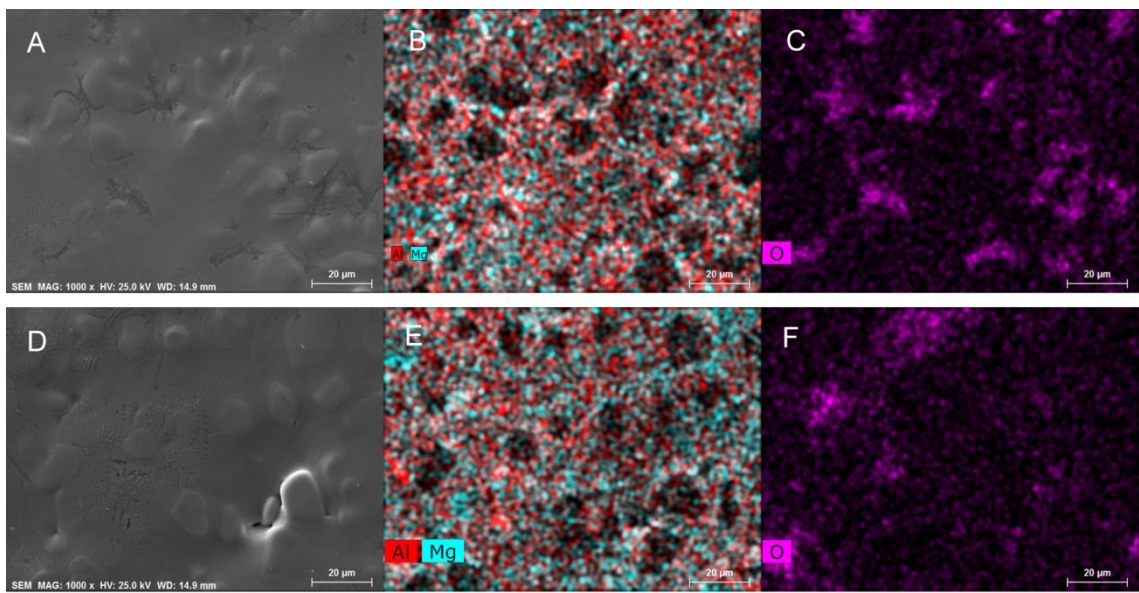


Figure 3. SEM micrographs and EDS maps of Al/Mg and O elements acquired on ZM(air) (a,b,c) and ZM(N2) (d,e,f) samples surface.

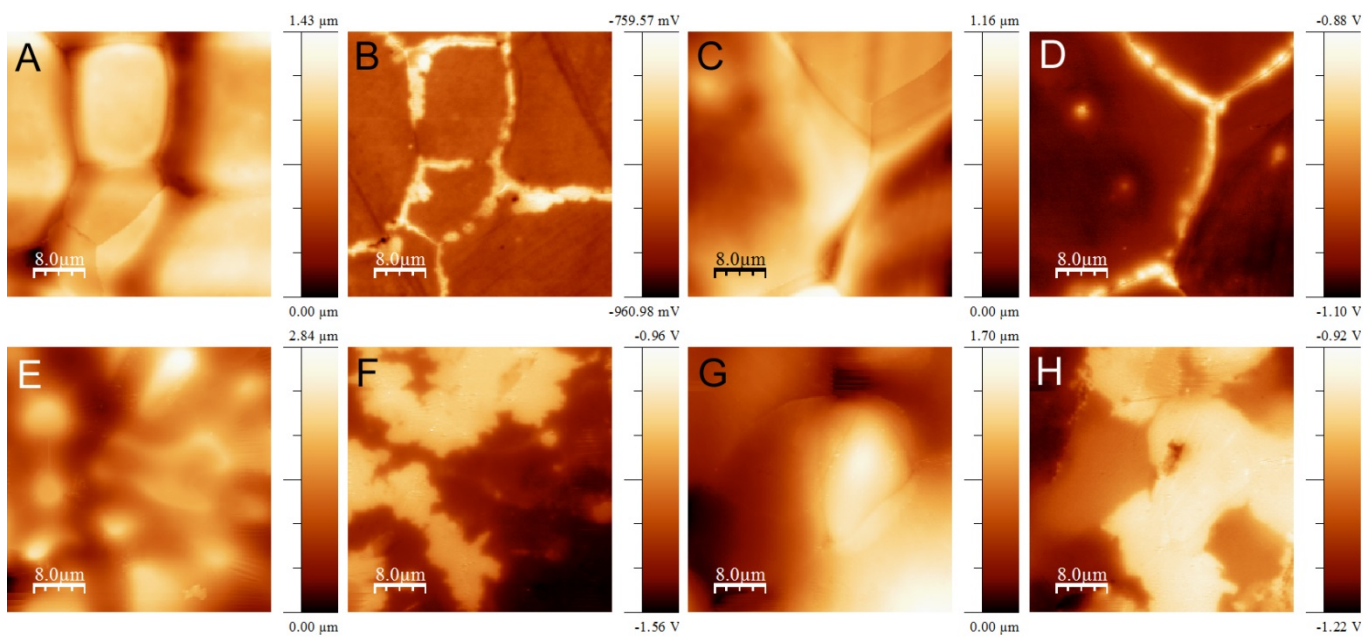


Figure 4. AFM (a,c,e,g) and SKPFM maps (b,d,f,h) of Z(air), (a, b), Z(N₂) (c, d), ZM(air) (e, f) and ZM(N₂) (g, h).

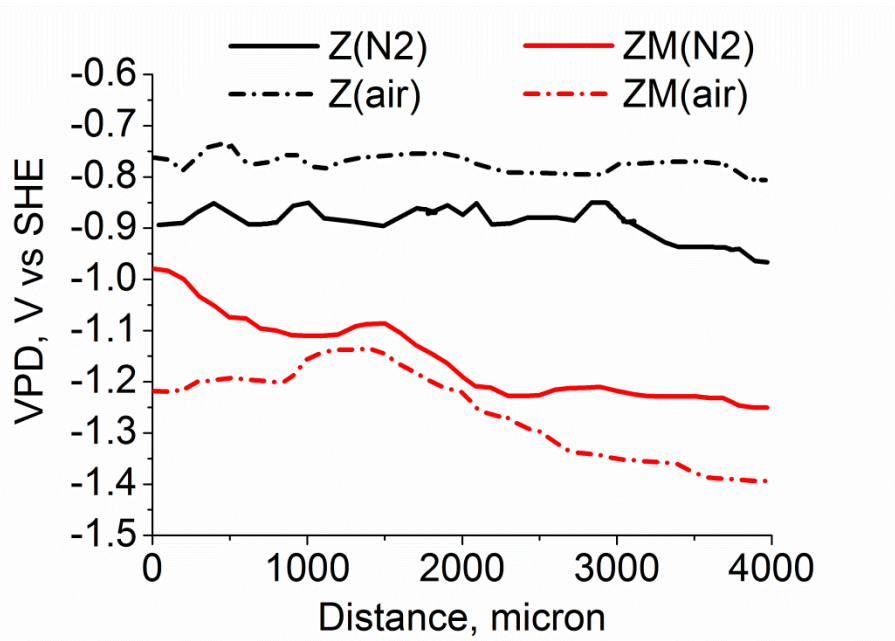


Figure 5. Scanning Kelvin Probe potentials of Z and ZM specimens prepared under air and N₂ atmospheres.

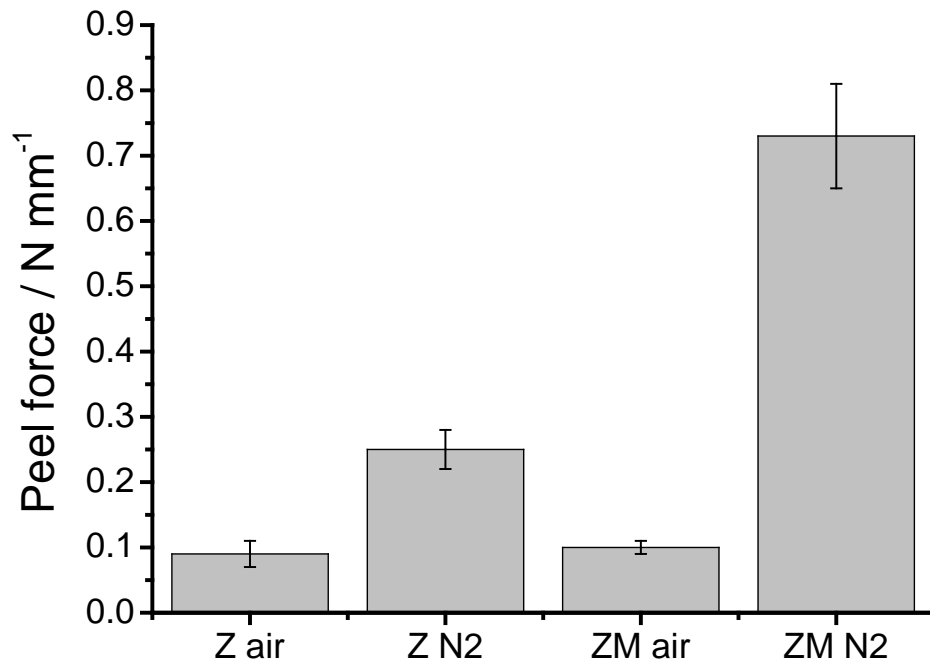


Figure 6. Peel forces measured on different substrates coated with adhesive layers.

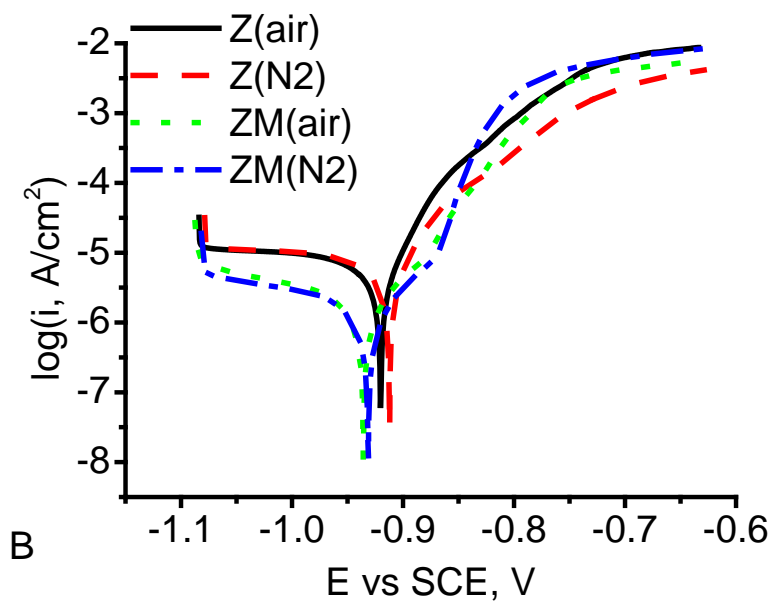
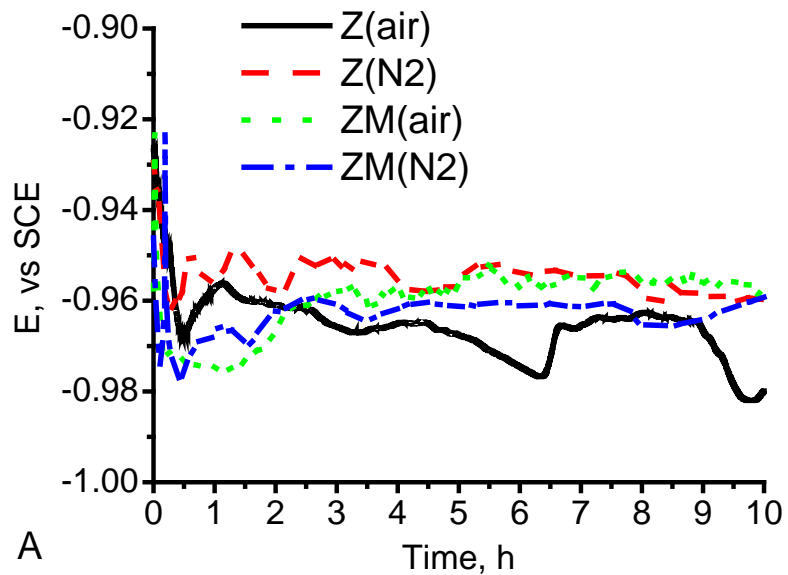


Figure 7. OCP evolution (a) during immersion in 5 mM NaCl solution; representative DC polarisation curves (b) acquired on Z and ZM samples after 0.5 h immersion in 5 mM NaCl solution.

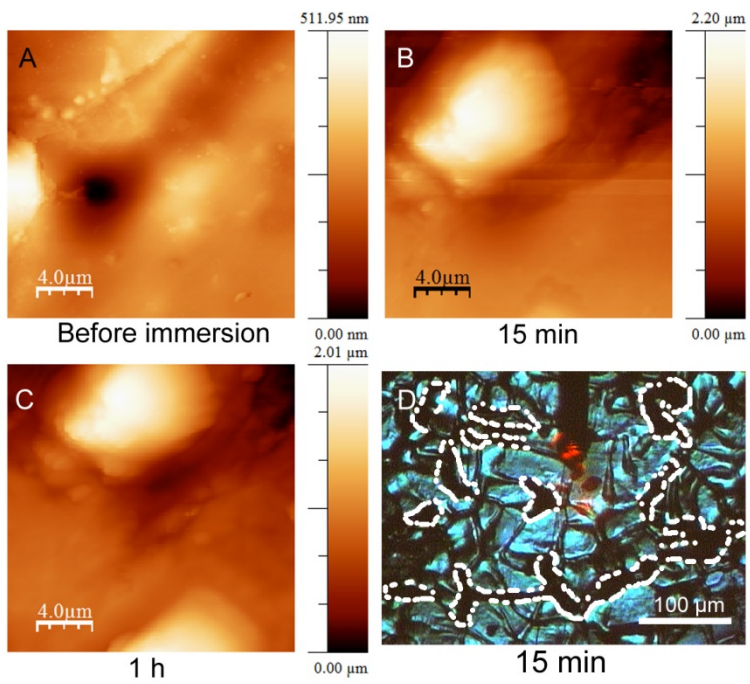


Figure 8. AFM maps (a,b,c) and surface optical picture (d) obtained on Z(air) sample during immersion in 5 mM NaCl.

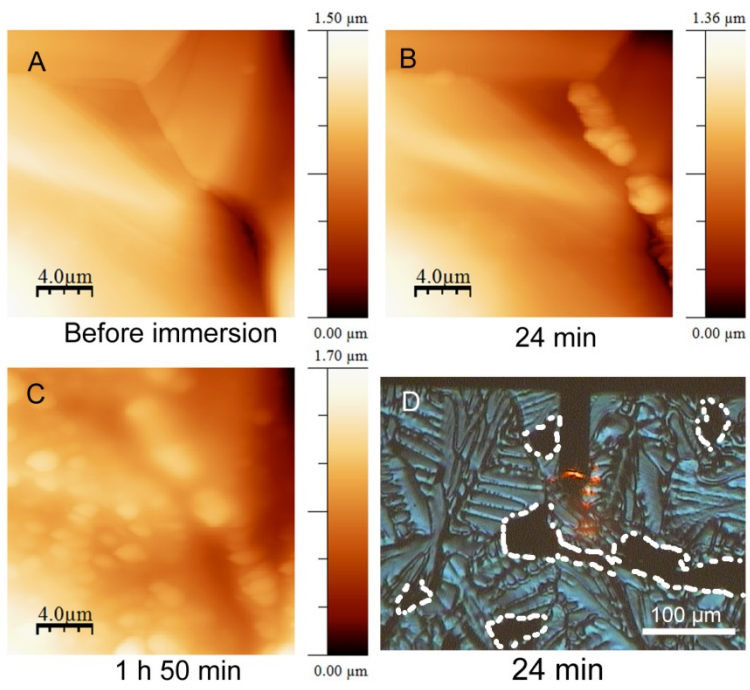


Figure 9. AFM maps (a,b,c) and surface optical picture (d) obtained on Z(N₂) sample during immersion in 5 mM NaCl.

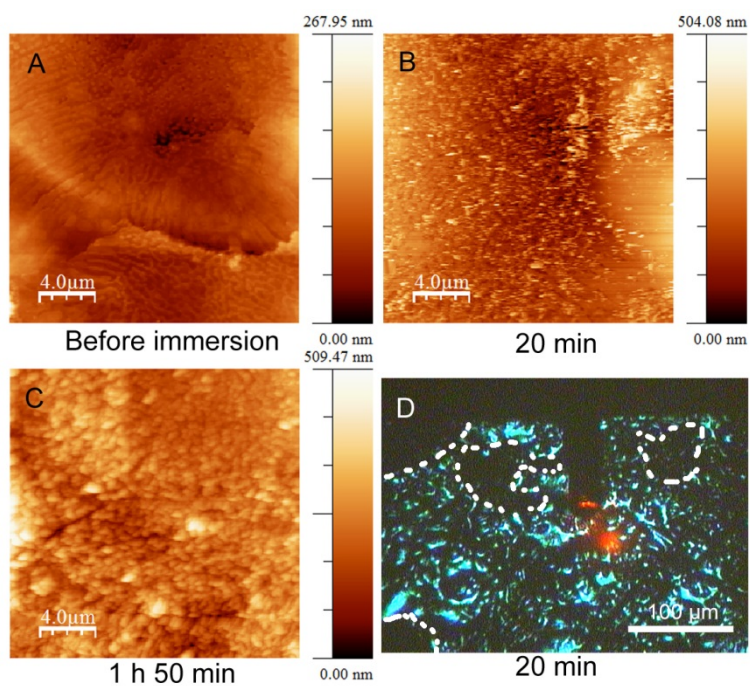


Figure 10. AFM maps (a,b,c) and surface optical picture (d) obtained on ZM(air) sample during immersion in 5 mM NaCl.

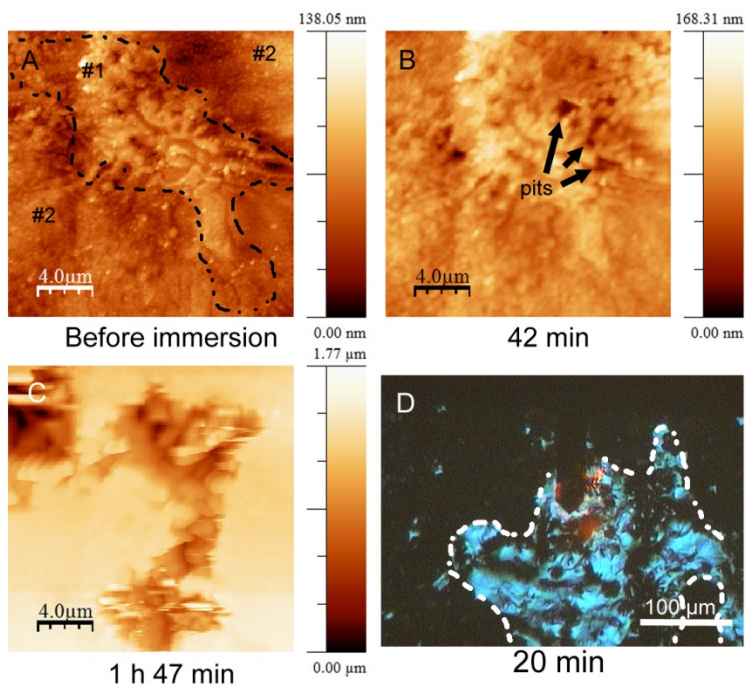


Figure 11. AFM maps (a,b,c) and surface optical picture (d) obtained on ZM(N2) sample during immersion in 5 mM NaCl.

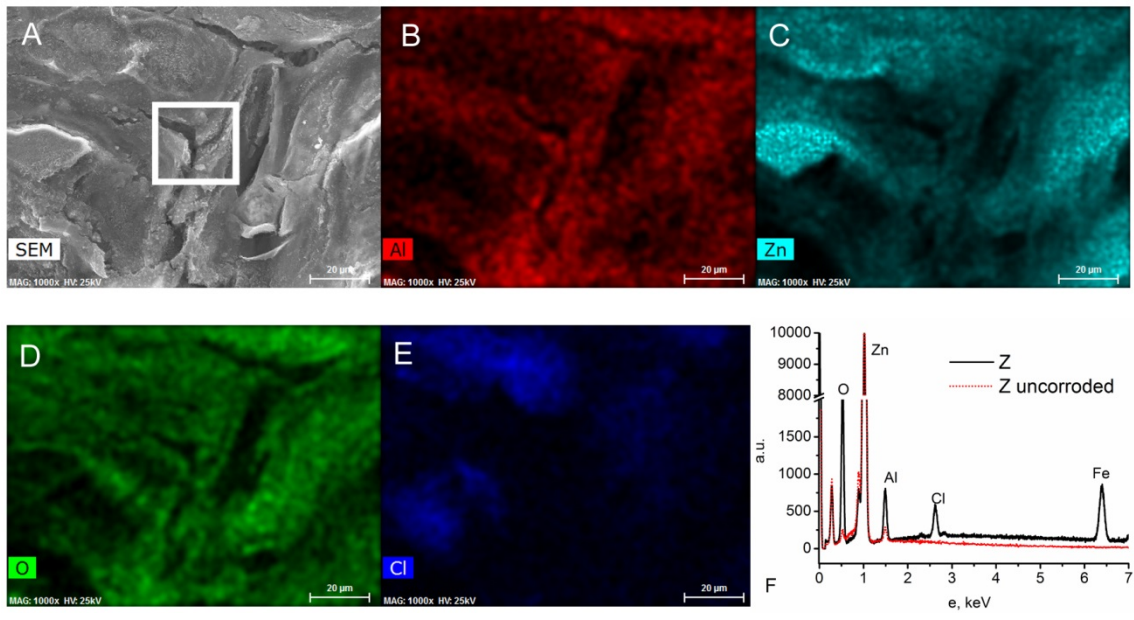


Figure 12. SEM and EDS analysis of Z(air) sample surface after 2h corrosion. The square corresponds to the area presented in Figure 8.

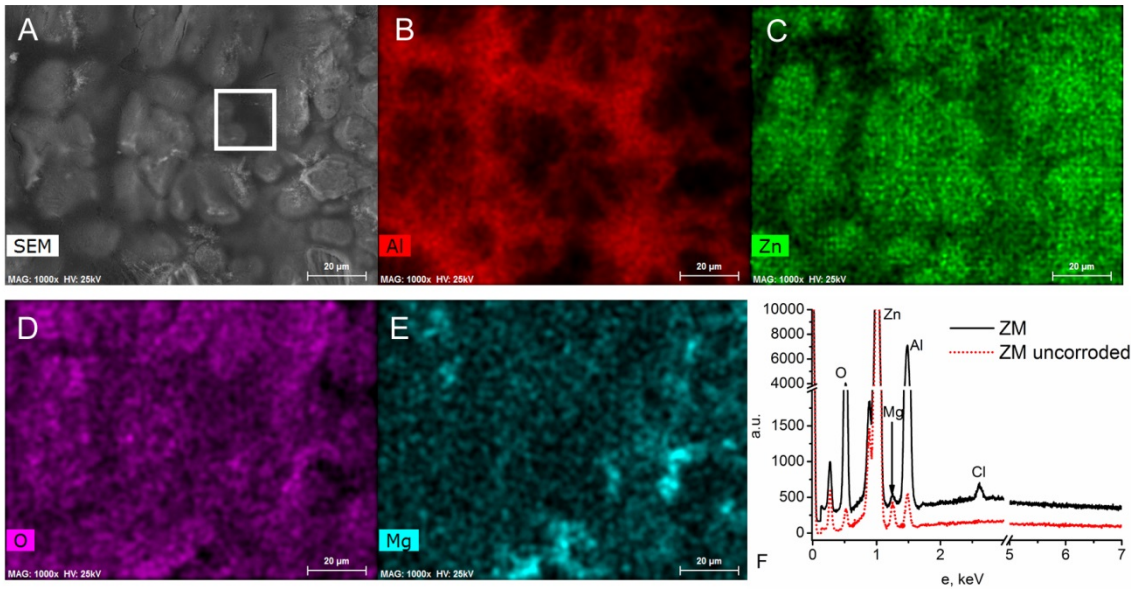


Figure 13. SEM and EDS analysis of ZM(air) sample surface after 2h corrosion. The square corresponds to an area presented in Figure 10.